

Visual anemometry for physics-informed inference of wind

John O. Dabiri^{1,2}✉, Michael F. Howland³, Matthew K. Fu¹ & Roni H. Goldshmid¹✉

Abstract

Accurate measurements of atmospheric flows at metre-scale resolution are essential for many sustainability applications, including optimal design of wind and solar farms, navigation and control of air flows in the built environment, monitoring of environmental phenomena such as wildfires and air pollution dispersal, and data assimilation into weather and climate models. Measurement of the relevant multiscale wind flows is inherently challenged by the optical transparency of the wind. This Perspective article explores new ways in which physics can be leveraged to ‘see’ environmental flows non-intrusively, that is, without the need to place measurement instruments directly in the flows of interest. Specifically, although wind itself is transparent, its effect can be seen in the motion of objects embedded in the environment and subjected to wind – swaying trees and flapping flags are commonly encountered examples. We survey emerging efforts to accomplish visual anemometry, the task of quantitatively inferring local wind conditions on the basis of the physics of observed flow–structure interactions. Approaches based on first-principles physics as well as data-driven, machine learning methods will be described, and remaining obstacles to fully generalizable visual anemometry are discussed.

Sections

Introduction

Principles of flow–structure interactions

Physics-based methods

Data-driven methods

Theoretical constraints on visual anemometry

Outlook

¹Graduate Aerospace Laboratories, California Institute of Technology, Pasadena, CA, USA. ²Mechanical and Civil Engineering, California Institute of Technology, Pasadena, CA, USA. ³Civil and Environmental Engineering, Massachusetts Institute of Technology, Cambridge, MA, USA. ✉e-mail: jodabiri@caltech.edu; ronigoldshmid@gmail.com

Introduction

The fate of life on Earth depends on physical processes that are macroscopic, but nonetheless imperceptible to the naked eye. Specifically, the movement of air masses at local scales mediates essential gas exchanges between the atmosphere and the terrestrial and aquatic ecosystems that lie underneath^{1–8}. This flow of air is also a principal means of transportation for life ranging from bacteria⁹ and seed spores^{10–14} to animals that migrate seasonally across the globe^{15–17}. Engineering technologies with the promise to protect those same ecosystems are also dependent on the wind. The functional reliance of technologies such as wind turbines is a straightforward example^{18–20}; however, it may be less appreciated that the performance of solar energy farms is also determined by local wind conditions^{21,22}. Boxes 1–3 provide further discussion of the diverse roles of wind flows in environmental sustainability applications.

Given this broad and important role of the wind for current and future environmental sustainability, it is remarkable that there are relatively few tools to quantify the wind at the length scales and timescales relevant to many of the applications identified earlier. Such measurements are inherently limited by the optical transparency of the air. To date, the most common solutions to this limitation require introducing an engineered, physical object into the flow whose interaction with the wind can be detected visually as a qualitative indicator (a windsock or wind vane²³, for example) or alternatively, by converting the physical interaction of the object and the wind into a calibrated, quantitative signal (using a cup anemometer or light detection and ranging system^{24–26}, for example). Measurements using these approaches are all fundamentally constrained by the requirement that the measurement device must be in close proximity to the measurement domain of interest.

This Perspective article explores an emerging alternative approach with the potential to enable multiscale, spatiotemporally resolved measurements of the wind by taking advantage of trillions of wind indicators already covering most of the land on Earth. These indicators include naturally occurring structures, such as the estimated three trillion trees on land²⁷, and engineered structures, such as the millions of kilometres of electrical power lines²⁸. Because none of these objects is perfectly rigid, they move in response to local wind conditions in ways that could potentially be used to infer incident wind speed and direction. We call this technique visual anemometry, reflecting the opportunity to quantify local winds based solely on visual measurements at arbitrarily far, line-of-sight distances away from the region of interest.

As a qualitative tool, visual anemometry has a long history and was first popularized in 1805 with the eponymous scale introduced by Francis Beaufort, a British naval officer, to standardize assessments of the effect of wind loading on ship sails. Subsequently adapted to wind over land, the Beaufort scale categorizes wind speed according to its qualitative effect on objects in the environment, from the gentle fluttering of leaves in low winds to the swaying motion of entire trees in high winds^{29,30}. Companion scales have subsequently been developed to categorize higher wind speeds, such as the Fujita scale for tornadoes³¹; time-averaged wind speeds over longer periods are categorized by the Griggs–Putnam index³². The distinct objective of this Perspective article is to explore the convergence of physics and data science to achieve visual anemometry that is quantitative in its assessment of the observed flow–structure interactions and generalizable to any structures that exhibit a visible response in the presence of wind. The content of this Perspective article is complemented by previous surveys of flow anemometry more generally³³, as well as reviews of the fluid

mechanics of urban canopies³⁴, plant canopies^{13,35}, forest canopies³⁶ and aquatic canopies³⁷.

We begin with an introduction to the relevant physics governing flow–structure interactions of the type expected to occur in wind flows. We then review current approaches towards visual anemometry, both physics-based and data-driven. We then highlight remaining challenges to successful realization of this method. We conclude by identifying diverse ways in which the physics community can contribute their disciplinary expertise to the development of this emerging field.

Principles of flow–structure interactions

Physics of vortex-induced vibration

Relative motion between a solid body and a surrounding fluid (Fig. 1a) creates lift forces, F_L , and drag forces, F_D , that act on the body (Fig. 1b). The lift force acts in the transverse direction of the fluid flow and has magnitude

$$F_L = \frac{C_L}{2} \rho U^2 A, \quad (1)$$

in which ρ is the fluid density, U is the incoming fluid speed, A is the relevant body area and C_L is the dimensionless lift coefficient. The drag force acts in the streamwise direction of the fluid flow, with magnitude

$$F_D = \frac{C_D}{2} \rho U^2 A, \quad (2)$$

in which C_D is the dimensionless drag coefficient. The magnitude of the lift and drag coefficients in an incompressible flow depends on the relevant Reynolds number (Re) of the body, in addition to the body shape and orientation in the flow. Per convention, Re is defined as $Re = \rho UL/\mu$, in which L is the relevant body length scale and μ is the dynamic viscosity of the fluid. Although C_L and C_D are nearly constant and on the order of 0.1–1 for rigid, bluff bodies at $Re \gg 1$, these coefficients can change and often decrease considerably with increasing flow speed, as discussed subsequently. Lift and drag forces are responsible for momentum exchange between the fluid (such as the surrounding air) and the body. When the body motion is coincident with one or both forces, the body extracts kinetic energy from the fluid.

A simple example of this energy transference (or harvesting) occurs when a bluff body is placed in a steady (that is, time-independent) flow. Across a wide range of flow conditions, these bodies generate an unsteady (that is, time-varying) wake characterized by periodic vortex shedding – the formation of spatially compact regions of rotating fluid downstream of the body – at formation frequency f_o . This vortex formation results in a spatially uneven pressure distribution on the body. For a body with a single degree of freedom, such as an elastic cantilever that is allowed to move in the transverse direction (Fig. 1a), this unsteady forcing causes the structure to respond by oscillating with so-called vortex-induced vibrations (VIVs). When the forcing frequency, f_o , from the vortex shedding approaches the natural frequency, f_n , of the structure, the dynamics of the two systems can become coupled in a state of synchronization or ‘lock-in.’ This resonant state is characterized by a considerable transfer of kinetic energy from the fluid to the structure resulting in large-amplitude oscillations. In this context, ‘large amplitude’ means that the oscillations are comparable to the characteristic length scale of the body cross-section. This mechanism is responsible for phenomena such as ‘singing’ wires and for the notable failure of the Ferrybridge cooling towers³⁸ in England. VIVs are one of many flavours of flow-induced vibrations,

Box 1

Visual anemometry for renewable energy

To achieve net-zero greenhouse gas emissions in the USA by 2050, it is estimated that increases in wind and solar capacity of 6–28× and 9–39×, respectively, are required¹⁵⁰; similarly large increases in renewable energy are needed globally to meet decarbonization targets. This unprecedented scale-up will require widespread proliferation of wind and solar generation in geographic regions where renewables have not previously been sited^{20,151}. Diversified siting of renewable energy infrastructure creates two main challenges related to wind measurements. First, wind patterns are more uncertain in new locations that have shorter historical observation records. Second, new sites may have lower quality wind, with characteristics that are more difficult to incorporate into existing forecasting methods, such as terrain complexity^{105,106,152,153} and variable land use (such as urban environments).

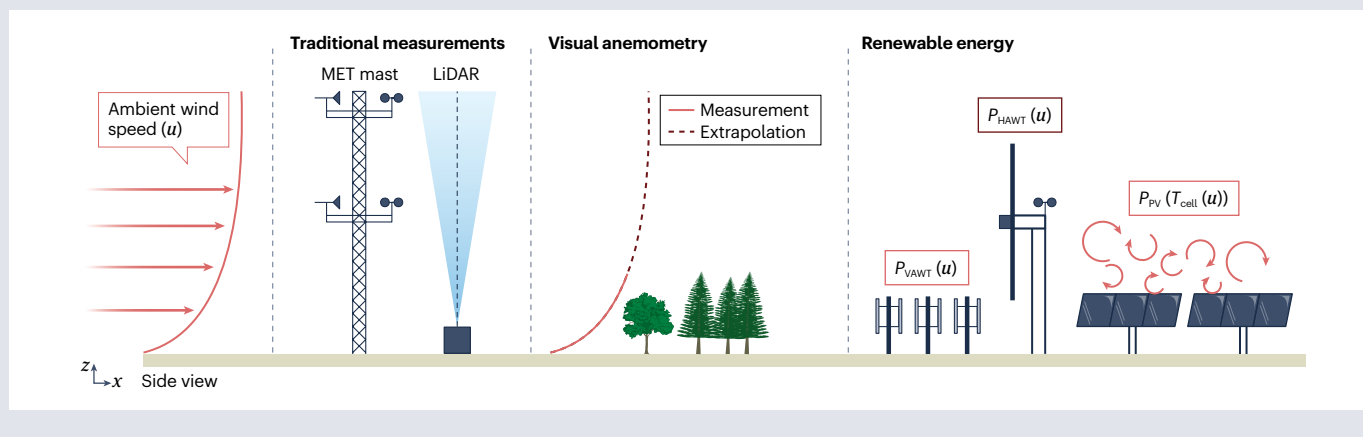
Historically, two parallel approaches have been used for wind field estimation for renewable energy resource assessment. The first is to predict the winds in the atmosphere via numerical weather forecasting models on the basis of an approximate form of the governing equations¹⁵⁴. These models require parameterizations to represent complex processes that cannot be directly resolved with available computing resources, such as turbulence, convection and clouds. Although numerical weather models provide detailed spatial and temporal coverage, the approximations in the models result in uncertainties in wind forecasts¹⁵⁵, especially near the surface of the Earth where turbulence is higher than aloft. In the second approach, in situ sensors such as meteorological (MET) masts and light detection and ranging (LiDAR) systems are used to observe the wind with few, if any, assumptions required regarding the nature of the wind dynamics^{33,105,156,157}. Yet these sensors both are relatively high cost and lack spatial coverage. At the intersection of these parallel approaches, data assimilation is used to combine in situ observations with numerical models^{158–160}, but uncertainties remain in locations not covered by the measurements. Visual anemometry can provide a third, complementary approach to wind field estimation with characteristics similar to in situ observations, but with higher spatial coverage. A promising avenue may

also leverage wind estimates from visual anemometry for data assimilation.

As most physical objects to be used for visual anemometry, both natural and engineered, exist within tens of metres of the surface of the Earth, measurements via visual anemometry directly quantify winds near this nominal height (see the figure). Small-scale wind generators, such as recently developed vertical-axis wind turbines (VAWTs), are designed with hub heights in the order of 10 m (ref. 161), making visual anemometry measurements directly applicable to the design of those systems. However, utility-scale horizontal axis wind turbines (HAWTs) operate at hub heights of 50–200 m and with rotor diameters of 80–300 m. For wind measurements made through visual anemometry to be used to estimate the power (P) available in winds incident to these utility-scale horizontal axis turbines, model-based extrapolation methods must be used¹⁶². Wind extrapolation to heights above a given measurement location is common, as typical weather stations also provide wind measurements 10 m above the surface of the Earth and surface winds reported by typical weather and climate models are also at 10 m.

Solar power production primarily depends on spatiotemporal variations in irradiance. Irradiance is driven by known deterministic variations, such as seasonal and diurnal cycles, as well as stochastic variations of atmospheric clouds and aerosols that are challenging to predict. Therefore, physics-based irradiance forecasts rely on numerical weather prediction¹⁶³. As noted earlier in the context of wind energy, visual anemometry may provide a mechanism for improved weather forecasting by increasing the availability of wind flow measurements for data assimilation.

Beyond irradiance, the efficiency of solar photovoltaic (PV) cells is rated at standard test conditions of one Sun of irradiance at an air–mass ratio of 1.5 (that is, sunlight passing obliquely through the equivalent of 1.5× the atmospheric length at zenith) and a cell temperature of $T_{\text{cell}} = 25\text{ °C}$. Yet PV cells typically operate at higher temperatures¹⁶⁴. Solar PV efficiency decreases by approximately 0.1–0.5% per Kelvin above standard test conditions, but the magnitude of degradation is cell-specific¹⁶⁵.



(continued from previous page)

To estimate efficiency in field conditions, solar cell manufacturers provide a method to approximate the cell temperature on the basis of an empirical indicator called the nominal operating cell temperature. Wind speed is a required input to this cell temperature approximation¹⁶⁶. Improving wind estimates increases the accuracy

of cell temperature and cell efficiency predictions¹⁶⁷. Finally, emerging research seeks to optimally site and design solar farms to maximize passive convective cooling to reduce cell temperature¹⁶⁸. Such methods require site-specific wind estimates²², which may be provided by visual anemometry.

along with aeroelastic flutter instabilities³⁹ and galloping^{40,41}, both of which result from forcing owing to unsteady pitching. Each of these response modes is a visually perceptible indication of the local wind conditions.

Effects of flexibility and reconfiguration

For relatively rigid structures whose shape does not change owing to wind forcing, the scaling in equations (1) and (2), especially the quadratic dependence on wind speed, adequately describes the behaviour of aerodynamic forces exerted by the wind. However, many naturally occurring structures, especially plants, are highly flexible and thus can deform considerably under forcing from external fluid flow (Fig. 1). Consequently, for many bodies, their flexural rigidity has an important role in determining the fluid forcing⁴². Because of this flexibility, many plants reconfigure their cross-section area and become more streamlined in higher speed flows, allowing them to experience a drag force with subquadratic dependency on flow speed⁴³. This dependency can be expressed as $F_D \propto U^{2+V}$, in which V is the Vogel exponent^{42,44–49}. Values of the Vogel exponent $V < 0$ capture the deviation from the canonical, inertial scaling relation owing to reconfiguration. For example, $V = -1$ indicates a regime in which drag scales near linearly with velocity. Depending on the mechanics of the reconfigurability, system-specific parameterizations have been used to quantify reconfiguration in previous studies (reviewed elsewhere⁴²). As discussed in the following sections, a goal of visual anemometry is to infer the relationship between structural response and incident wind without an a priori model of reconfiguration dynamics.

Effects of biological adaptation

The preceding discussion of reconfiguration implicitly assumes that the reconfiguration of the structure exposed to wind is reversible; in other words, that the original configuration of the structure is recovered when wind loading is removed. Although this is typically true for engineering structures, provided that they are not stressed beyond the limits of elastic deformation, vegetation can exhibit a more complex response to wind loading. Specifically, many plants exhibit structural remodelling – at a cellular level – in response to wind loading that leads to different equilibrium geometries of the vegetation over time^{50,51}. Hence, the structure of vegetation can encode the time history of previous exposure to wind loading. If not properly accounted for, this adaptation can potentially confound efforts towards visual anemometry, as two plants of the same species but with different wind-loading histories could respond differently to incident wind, if one has grown stiffer owing to previous exposure to the wind, for example.

Conversely, by recognizing the occurrence of this phenomenon, a type of adaptation known as thigmomorphogenesis⁵², additional information regarding the wind conditions can be beneficially leveraged in the task of visual anemometry. For example, the long-term deformation of trees has previously been exploited for the estimation

of average annual wind speeds³² and even for siting of wind turbines⁵³. Hence, knowledge of the phenotypic plasticity of a given vegetation species (such as its capacity for thigmomorphogenesis) along with measurement of its equilibrium structure can complement visual observations of the instantaneous flow–structure interactions. The following section focuses on the physics governing the flow–structure interactions. Strategies to incorporate additional information regarding vegetation species and wind history (such as information inferred from the observed equilibrium structure of the vegetation) are discussed in the subsequent section on data-driven methods.

Physics-based methods

Dynamics-based methods

Physical objects that are both geometrically slender and mechanically stiff have proven the most amenable to direct, first-principles application of flow physics to deduce a quantitative relationship between object motion and incident wind speed. In these cases, the aerodynamic force of the wind on the structure can be estimated as $F_{\text{wind}} \approx \bar{p}A$, in which \bar{p} is the dynamic pressure exerted by the wind on the windward face of the structure, the overbar indicates a spatiotemporal average and A is the projected area of the corresponding surface. Similar to the lift and drag forces described in equations (1) and (2) mentioned earlier, the dynamic pressure is linearly proportional to the air density and quadratically proportional to the incident wind speed; hence,

$$F_{\text{wind}} \propto \rho \bar{U}^2 A. \quad (3)$$

The structural response to small deformations can be estimated by assuming that the elastic restoring force, F_E , is linearly proportional to the structure deflection δ :

$$F_E \approx \kappa \delta, \quad (4)$$

in which κ is the elastic constant, which depends on the structure geometry and material properties. For cantilevered, slender objects such as tree branches, plant stalks or blades of grass, the tip deflection owing to spatially uniform wind loading can be modelled using the linear Euler–Bernoulli beam theory:

$$\delta \approx \frac{fL^4}{8EI}, \quad (5)$$

in which f is the applied force per unit length L , E is the elastic Young's modulus of the material comprising the structure and I is the area moment of inertia. Comparing equations (4) and (5) mentioned earlier, the corresponding elastic constant is

$$\kappa \approx \frac{8EI}{L^3}. \quad (6)$$

The balance of aerodynamic force, F_{wind} , and elastic force, F_E , provides a relationship between observed structural deflection and incident wind speed:

$$\bar{U} \approx \sqrt{\frac{8EI\delta}{\rho AL^3}}. \quad (7)$$

Each of the parameters on the right-hand side of equation (7) can be estimated from visual observation of the structure, with the exception of the Young's modulus of the material. Reference⁵⁴ demonstrated the use of single-point calibration to determine the unknown material property. Alternatively, computer vision techniques can potentially be used to deduce the likely material properties on the basis of libraries of environmentally observed structures and their known material properties^{55,56}.

An important limitation of methods based on the preceding analysis is the necessary occurrence of a non-zero time-averaged structural deflection owing to the incident wind. As described earlier, the VIVs experienced by many environmental structures, such as plants⁵⁷, can exhibit a mean deflection that is close to zero, despite significant instantaneous deflections. The oscillatory motion of electrical power lines under wind loading is another common example; other engineered structures, such as telephone poles and radio antennae, can also exhibit nearly symmetric structural oscillations in a direction perpendicular to the incident wind²⁸.

Reference⁵⁸ showed that the dynamic motions associated with transverse or streamwise structural oscillations can also be used to estimate wind speeds, albeit using a conceptual framework different from the quasi-steady force balance that leads to equation (7). In this

case, the dynamics of the flow–structure interaction are modelled as a damped harmonic oscillator:

$$F_{\text{wind}}(t) \approx m \frac{d^2\delta}{dt^2} + \lambda \frac{d\delta}{dt} + \kappa\delta, \quad (8)$$

in which m is the structure mass, λ is the damping coefficient of the structure and the last term on the right-hand side of the equation is the elastic response analysed previously. In principle, any time-dependent wind forcing can be represented as a superposition of harmonic forcings⁵⁹ at a spectrum of frequencies:

$$F_{\text{wind}}(t) = \frac{a_0}{2} + \sum_{n=1}^N (a_n \cos nt + b_n \sin nt) \quad (9)$$

in which a_n and b_n are constants, and the summation includes N modes sufficient to approximate the time dependence of the incident wind. For harmonic forcing at a single frequency ω , in other words, $F_{\text{wind}}(t) = F_0 \sin \omega t$, equation (8) has the steady-state solution⁵⁸:

$$\delta(t) = \frac{F_0}{\kappa} \left[\frac{1}{(1-\beta^2) + (2\zeta\beta)^2} \right] [(1-\beta^2)\sin(\omega t) - 2\zeta\beta \cos(\omega t)], \quad (10)$$

in which β is the ratio of the forcing frequency to the natural frequency of the structure, and

$$\zeta = \frac{\lambda}{\sqrt{4\kappa m}}. \quad (11)$$

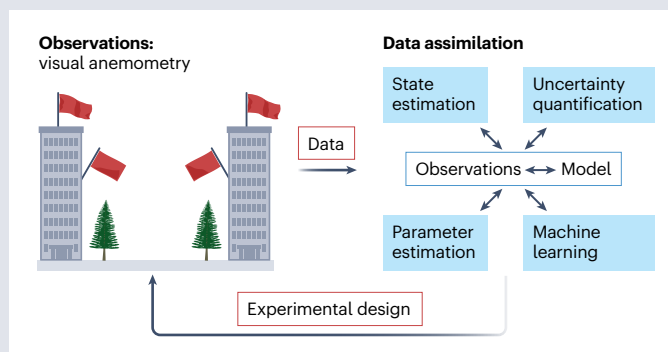
Box 2

Visual anemometry for urban airflows

People increasingly live in urban environments. In recognition of this important trend, the [United Nations Sustainable Development Goal 11](#) focuses on sustainable cities and communities. Air flow in urban environments affects the energy efficiency and resilience of engineered structures, pollution dispersion and air quality, and the future of urban air mobility. Given the broad impacts of urban air flow, and the limited fidelity of present observations and predictive models, urban air flow represents a grand challenge in environmental fluid mechanics¹⁶⁹.

Air flow affects the structural resilience and energy efficiency of buildings. Design standards incorporate site-specific wind characteristics, including extreme wind gusts¹⁷⁰, which are difficult to measure or numerically model. Urban airflow also affects thermal convection in cities, which impacts the energy consumption of building heating and cooling systems, and the effectiveness of natural ventilation¹⁷¹.

Finally, the design of future aircraft and airspace for urban air mobility depends on our ability to predict the turbulent flow within and around urban environments¹⁷². Safe and reliable transport of people and goods requires detailed knowledge of wind gusts and turbulence, as contemporary aircraft control methods have less success in navigation and object avoidance in uncertain wind environments¹⁷³.



Flows in urban environments are heterogeneous and complex; these traits reduce the accuracy of numerical flow predictions and severely limit the accuracy of spatially extrapolated pointwise flow field measurements. There is an urgent need for increased spatiotemporal coverage of urban air flow measurements¹⁶⁹ for both validation and uncertainty quantification of numerical models^{174,175} as well as for data assimilation¹⁷⁶. Visual anemometry can provide a new approach for urban wind field sensing with wide spatial coverage and high spatiotemporal resolution (see the figure).

Box 3

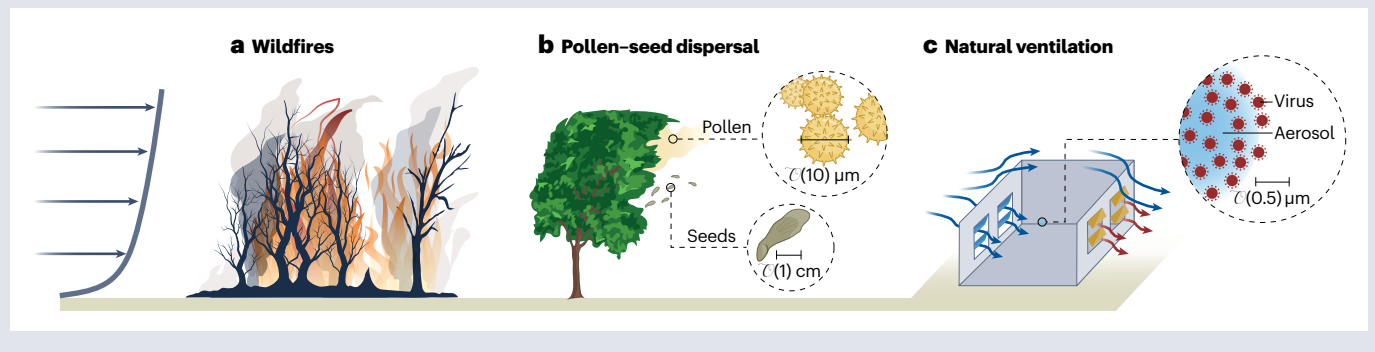
Visual anemometry for environmental and ecological processes

Transport, mixing and atmospheric conditions driven by the wind are central to numerous environmental and ecological processes. Wildfire prediction and mitigation (see the figure, panel **a**) are notable applications in which detailed wind mapping can have a critical role. In the USA alone, wildfires have cost an average of \$13.4B USD per year^{177,178} in damages in 2017–2022 and are predicted to become even more prevalent as warmer and drier conditions, driven by climate change, lead to more protracted and active fire seasons^{179,180}. Although temperature, humidity and stability conditions are critical contributors to the intensity of a wildfire, wind conditions have a leading role in determining the speed and direction of the wildfire spread^{181–183}. In chaparral ecosystems such as coastal Southern California, the regions most exposed to extreme wind events (such as the katabatic Santa Ana winds) have been linked to increased fire danger and larger fires^{184,185}.

Prevailing wind conditions and their associated turbulence also drive the dispersal of critical scalar quantities (such as heat and mass) and particulates central to various ecological and environmental processes (see the figure, panel **b**). Long distance dispersal of seeds¹⁴, spores¹⁸⁶ and pollen¹⁸⁷, whether by wind or organisms, is a critical yet poorly understood survival strategy^{11,14,188,189} for species that adapt to changing habitats by overcoming geographic isolation^{10,190,191}. Many of the world’s most important agricultural grains, including wheat, barley, corn and rice, are grasses that are pollinated primarily through the wind, owing to their lack of flowering structures¹⁹². Although such a mechanism is most prevalent for plants located in close proximity — within a range of 1 km¹⁹³, for example — airborne transport and mating of taller plants, such as trees, has been documented at distances exceeding 10 km^{12,187,194}. Understanding these dynamics is critical for ensuring or minimizing cross-pollination between various crops; the latter is especially critical to limit contamination from genetically

modified crops¹⁹³ in the natural environment. Even propagated material that is transported by organisms depends in part on wind dynamics for its dispersal. The efficacy of crop treatment by pesticides is also directly impacted by local wind conditions^{195–199} (see also [Herbicide Stewardship and Drift Prevention](#)). Current guidelines reflect an inability to precisely quantify the wind flows that carry pesticide chemicals, presenting another application of visual anemometry with broad impact.

Natural dispersal, convection and mixing by wind have similarly been leveraged by humans for various engineering purposes, including for pollution dispersal²⁰⁰ and natural ventilation^{201,202} (see the figure, panel **c**). Proper ventilation is necessary to ensure a healthy indoor environment, but it comes with a tangible energy cost. Ventilation comprises approximately 11% of the nearly 7 quadrillion BTU (2 million GWh) and \$USD 141 billion spent by commercial buildings in the USA alone²⁰³. This expenditure does not include the energy spent on space heating or cooling, which are both also substantial (32% and 8% of energy consumption by commercial buildings in the USA, respectively). Natural ventilation presents an efficient and largely passive alternative to conventional ventilation approaches. This approach uses naturally occurring forcing from wind and/or buoyancy to exchange air between the indoors and outdoors through openings in a building structure. Although this resource is freely available in appropriate climates, it can be challenging to control and predict^{204,205} owing to the inherent complexity and variability of the airflow inside connected rooms and around the structure^{206–208}. Designing a system to adequately take advantage of wind-driven forcing requires detailed knowledge of the turbulent wind patterns in and around the building across diurnal and seasonal variations²⁰⁹. This represents another potentially transformative application of visual anemometry.



Inspection of this steady-state solution indicates that the amplitude of the structural oscillations is directly proportional to the amplitude of the wind forcing. Appealing to the relationship between wind speed and forcing in equation (3) mentioned earlier, and with additional algebraic manipulation, reference⁵⁸ shows that, for typical, low levels of atmospheric turbulence, that is, if the turbulence intensity I_u is given by

$$I_u \equiv \frac{\sigma(U)}{U} \ll 1, \tag{12}$$

then

$$\bar{U} \propto \sqrt{\frac{\sigma(\delta)}{I_u}}, \tag{13}$$

in which σ denotes the standard deviation. Field measurements demonstrated that this relationship captures the flow–structure interactions of five tree species representing a diversity of morphologies^{58,60}.

As with the preceding mean deflection model, visual anemometry based solely on the physics of the time-dependent structural response

still requires a calibration measurement to determine the constant of proportionality in the relationship expressed by equation (13). This potentially limits visual anemometry to contexts in which one has a priori wind measurements using conventional anemometry techniques. To unlock the potential of visual anemometry for global coverage, especially in regions where conventional anemometry is inaccessible, dynamical models such as those mentioned earlier may require augmentation with other approaches.

Energy-based methods

Although the mechanical properties of a structure exposed to wind can be difficult to infer on the basis of visual observation of its isolated flow–structure interactions, the presence of multiple identical structures could be leveraged to infer their common properties. Consider, for example, the wind incident on two trees aligned in the streamwise direction. The discussion in the preceding sections indicates that the

kinetic energy of each tree is derived from the kinetic energy of the incident wind. For instance, for the upstream tree

$$KE_{T_1} \approx \eta KE_{\text{wind}}, \quad (14)$$

in which KE_{T_1} is the kinetic energy of the upstream tree, KE_{wind} is the kinetic energy of the wind incident on the front of the canopy and η is a constant factor that quantifies the energy transfer from the wind to the trees. This factor captures the mechanical properties of the tree, such as its inertia, elasticity and damping. A value $\eta = 0$ would indicate no energy transfer from the incident wind to the tree, whereas a value $\eta = 1$ would indicate the (unphysical) upper bound of perfect energy transfer from the wind to the tree. In practice, the maximum value of the energy transfer coefficient η is much less than 1. For example, in steady incompressible flow, the maximum theoretical value is given by the Betz limit of 59.3% (ref. 61). Unsteady flows can exhibit higher

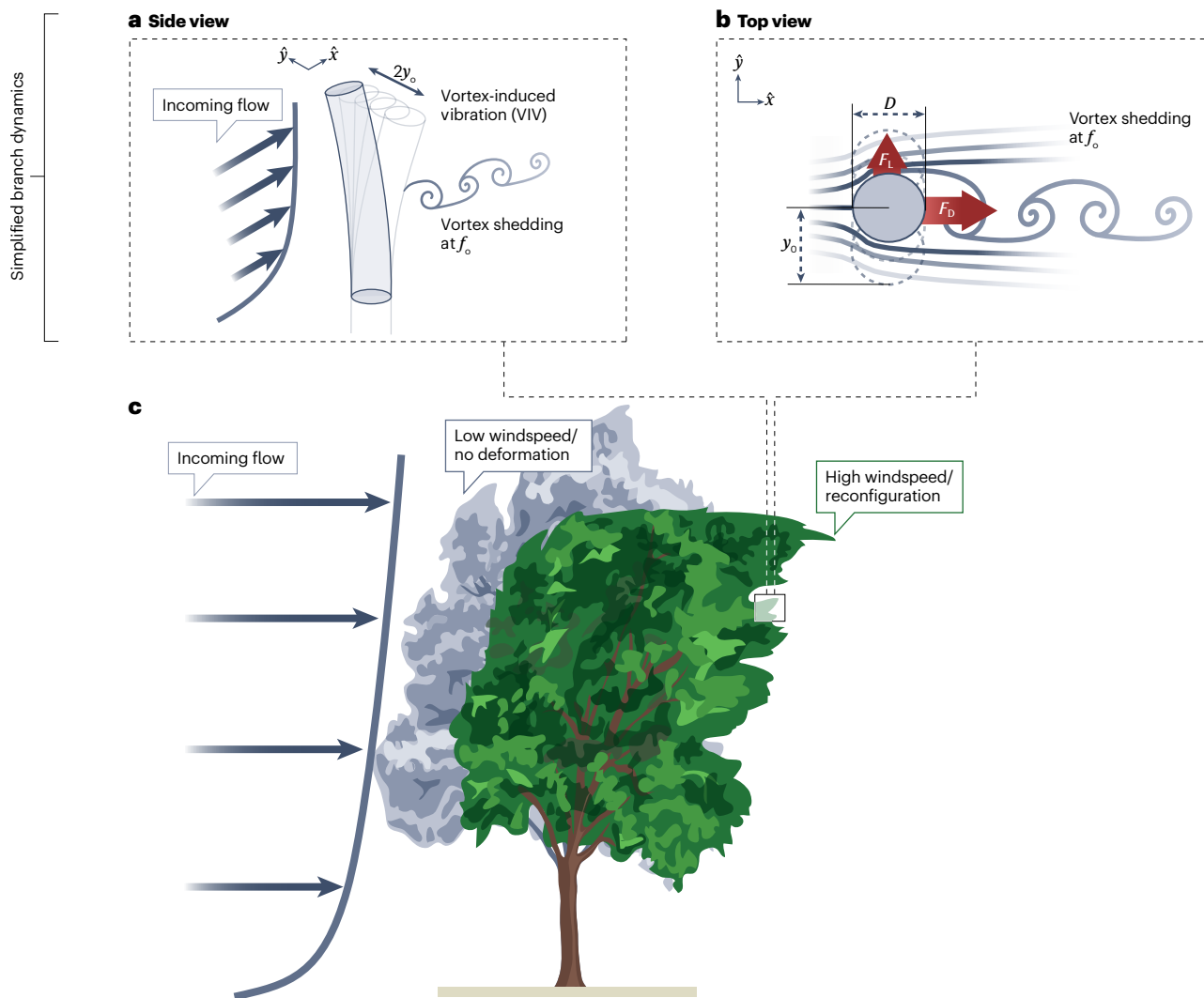


Fig. 1 | Physics of flow–structure interactions. **a, b**, Slender objects, such as the branches of a plant, can undergo VIVs in a direction transverse to the incoming flow (panel **a**), owing to vortex shedding and associated lift and drag forces (panel **b**). **c**, In high-speed flows, flexible structures such as vegetation can

undergo reconfiguration, which reduces proportional increases in aerodynamic forces from the wind. D , cylinder diameter; f_0 , formation frequency; F_L , lift force; F_D , drag force; y_0 , half-width of transverse displacement.

energy transfer efficiencies in theory, although empirical observations suggest that values less than the Betz limit are typical⁶².

If the second, downwind tree is set into motion solely by remaining kinetic energy in the wake of the first tree, that is, $KE_{\text{wake}_1} \equiv KE_{\text{wind}} - KE_{T_1}$, then we can estimate the kinetic energy of the second tree as

$$KE_{T_2} \approx \eta KE_{\text{wake}_1} \approx \eta(1 - \eta) KE_{\text{wind}}. \quad (15)$$

To be sure, this approximation assumes that no energy was dissipated in the interaction with the upstream tree (that is, that there is negligible damping on the timescale of wind advection), and it assumes that the upstream wind does not also directly affect the dynamics of the second, downwind tree, as might occur via turbulent sweeps into the top or sides of the canopy^{24,35,63,64} or a redistribution of the kinetic energy within its frequency spectrum⁶⁵, for example. In other words, this approximation depends inherently on the level of turbulence in the incident wind and on the surrounding topography.

We postulate that two trees (or other objects exposed to the wind) with identical structural properties are characterized by the same value of energy transfer efficiency η . With this ansatz, one can eliminate the unknown structural properties η by comparing the relative magnitude of the motion of the two trees:

$$\frac{KE_{T_1}}{KE_{T_2}} \approx \frac{1}{1 - \eta}, \quad (16)$$

or,

$$\eta \approx 1 - \frac{KE_{T_2}}{KE_{T_1}}. \quad (17)$$

The kinetic energy of each structure can be estimated as proportional to the average of the square of its component speeds. Hence,

$$\eta \approx 1 - \frac{\overline{U_{T_2}^2}}{\overline{U_{T_1}^2}}, \quad (18)$$

in which the carat denotes a spatial average of the structure motion. The model in equation (18) could be enhanced by incorporating more realistic functional dependencies of the parameter η , for example, to reflect possible sensitivity of the kinetic energy transfer efficiency to the wind speed (such as occurs via structure reconfiguration as discussed in the section on Effects of flexibility and reconfiguration) and background turbulence levels. However, these additions would potentially re-introduce the need for local calibration measurements. Even in its current form, equation (18) illustrates the potential for canopies comprising an array of similar structures to be especially useful for visual anemometry.

An additional physical phenomenon that can influence the accuracy of visual anemometry using the preceding energy-based methods is the presence of ‘honami’, that is, waves of wind-induced structural displacement that can propagate through a canopy^{66,67}. For canopy elements in close proximity, mechanical contact between upstream and downstream elements during wave propagation could lead to additional kinetic energy transfer between canopy elements. Because this transfer of kinetic energy can be two way – with energy transferred from upstream canopy elements to downstream or vice versa – the upstream energy

transfer could lead to underestimation of the wind kinetic energy transferred to downstream canopy elements and thereby underestimate η . For a uniform canopy, this should manifest as a systematic bias in the measurements. If so, then this artefact should be straightforward for a data-driven method to compensate on the basis of training data (as discussed in the sections on Data-driven methods and on Outlook).

Each of the aforementioned physics-based methods is fundamentally limited by the fidelity with which 2D visual observations of the vegetation motion can accurately quantify the actual 3D canopy kinematics^{47,68–70}. A top view of the canopy provides a projection of the two dominant wind directions (that is, streamwise and cross-wind), assuming that vertical wind flows are negligible, as in canonical horizontally homogeneous atmospheric surface layer flows⁶⁴. Hence, visual anemometry from this perspective is less sensitive to out-of-plane canopy motion that would cause the canopy kinetic energy to be underestimated. Moreover, because the vegetation is cantilevered at the ground, the portion of the canopy that is visible from overhead will typically exhibit the most significant displacements. This feature of overhead measurements becomes especially important for visual anemometry conducted from distant vantage points such as aircraft or satellites (as discussed further in the section on Outlook). The overhead perspective is also especially useful for inference of wind direction, which can be a desired output of visual anemometry irrespective of quantitative measurements of wind speeds.

Despite these advantages of overhead views of flow–structure interactions, many data sets of interest will necessarily be collected from ground-level perspectives, in which the canopy is viewed from the side. In these cases, visual anemometry can only capture the projection of the wind in the plane perpendicular to the optical axis. Moreover, the wind associated with the observed canopy motions will be primarily the wind at the lateral sides of the canopy, as that is the primary visible interface between the canopy and the surrounding wind from a side view. If the motion of the top of the canopy is visible from the side, then it may also be possible to estimate wind at the upper interface of the canopy and the wind. In that case, one can anticipate a vertical gradient with wind speeds increasing from the ground to the top of the canopy.

Ultimately, 3D canopy tracking, via light detection and ranging, for example, could obviate the need for these considerations, as 3D reconstruction of the canopy motion would eliminate the aforementioned projection errors.

Data-driven methods

The constants of proportionality needed to complete the physical relationships expressed in equations (7), (13) and (14) depend on factors specific to the objects being visually observed, such as their inertia, stiffness and damping. Non-intrusive measurement of these properties at the scale of individual environmental structures is challenging, if not impossible, particularly when those objects comprise a heterogeneous composite of multiple materials. A potential way forward is to use the fact that the trillions of environmental objects of interest globally can be classified into a set of material categories that is several orders of magnitude smaller in number. For example, building codes limit the set of allowable compositions of artificial structures to a relatively small number of engineered materials^{71,72}. These materials could therefore be deduced in many cases from the external appearance of the structures. As another example, high-voltage power lines are typically composed of an aluminium core and polyethylene insulation, both of standard physical dimensions^{73–76}. Hence, the material properties of such an environmental structure can be deduced as soon as it is categorized.

Naturally occurring structures such as vegetation present a greater challenge, given both the diversity of their physical makeup and the fact that structure inertia, stiffness and damping depend non-trivially on factors such as age, health, moisture content and the presence or absence of leaves, seeds and symbiotic organisms. Notwithstanding these myriad challenges, initial efforts towards data-driven visual anemometry have produced encouraging results^{77–79}. For example, a combined convolutional neural network and long short-term memory network has been trained on the basis of field observations of a magnolia tree and a cloth flag exposed to naturally occurring wind conditions over several weeks⁷⁷. It was postulated that the convolutional neural network learns to recognize key features of the objects exposed to the wind, such as tree branches and leaves, or geometric patterns on the flag. Concurrently, the long short-term memory was hypothesized to learn key temporal features of the object motion, such as recurring waving or flapping motions of the geometric patterns.

The trained neural network was subsequently tested on video clips of the same tree and flag that were not included in the training data set. This purely data-driven visual anemometry achieved measurements of the mean wind speed with errors comparable with the background turbulence fluctuations at the field site of approximately 1–2 m s⁻¹ (Fig. 2).

Because this purely data-driven, machine learning approach has limited capacity for extrapolation beyond the training data distribution⁷⁷, it was unable to perform similarly accurate predictions using videos of tree specimens or flag types different from those in the training data. Hence, a generalizable version of visual anemometry in this case, that is, a method that can make accurate measurements for a diversity of vegetation and engineered structures, would likely require training on a far more comprehensive set of videos and companion anemometer data. Brute-force efforts of this type have proven successful in the past, such as in the image classification projects ImageNet⁸⁰ and COCO⁸¹. However, developing the equivalent data set for visual anemometry would likely

require a combination of existing open-source data and new, dedicated measurement campaigns. We revisit this possibility below.

Theoretical constraints on visual anemometry

Generalized visual anemometry – a technique that does not require calibration measurements or a priori collection of training data – will depend on the discovery of new physical principles that manifest in predictable ways across a diversity of environmental structures exposed to wind. In pursuit of fundamental concepts of this type, we have recently conducted an extensive campaign of concurrent wind and visual measurements in a large-scale wind tunnel⁸². This facility enables controlled studies of selected vegetation with a diversity of morphologies, ranging from grasses to trees (Fig. 3).

The incident wind speed can be described by a two-parameter Weibull probability density function^{83,84}:

$$p(U) = \begin{cases} \frac{C_2}{C_1} \left(\frac{U}{C_1}\right)^{C_2-1} e^{-\left(\frac{U}{C_1}\right)^{C_2}}, & U \geq 0 \\ 0, & U < 0 \end{cases} \quad (19)$$

in which C_1 is a positive-valued, dimensional scale factor that increases for distributions $p(U)$ with higher variance. The dimensionless shape factor C_2 typically takes values between 1 and 3 for wind distributions, with values closer to 1 indicating right skewness of the distribution⁸³. Moments of the Weibull distribution can be expressed in terms of C_1 and C_2 ; for example, the mean wind speed is given by

$$\bar{U} = C_1 \Gamma\left(1 + \frac{1}{C_2}\right), \quad (20)$$

in which Γ is the gamma function.

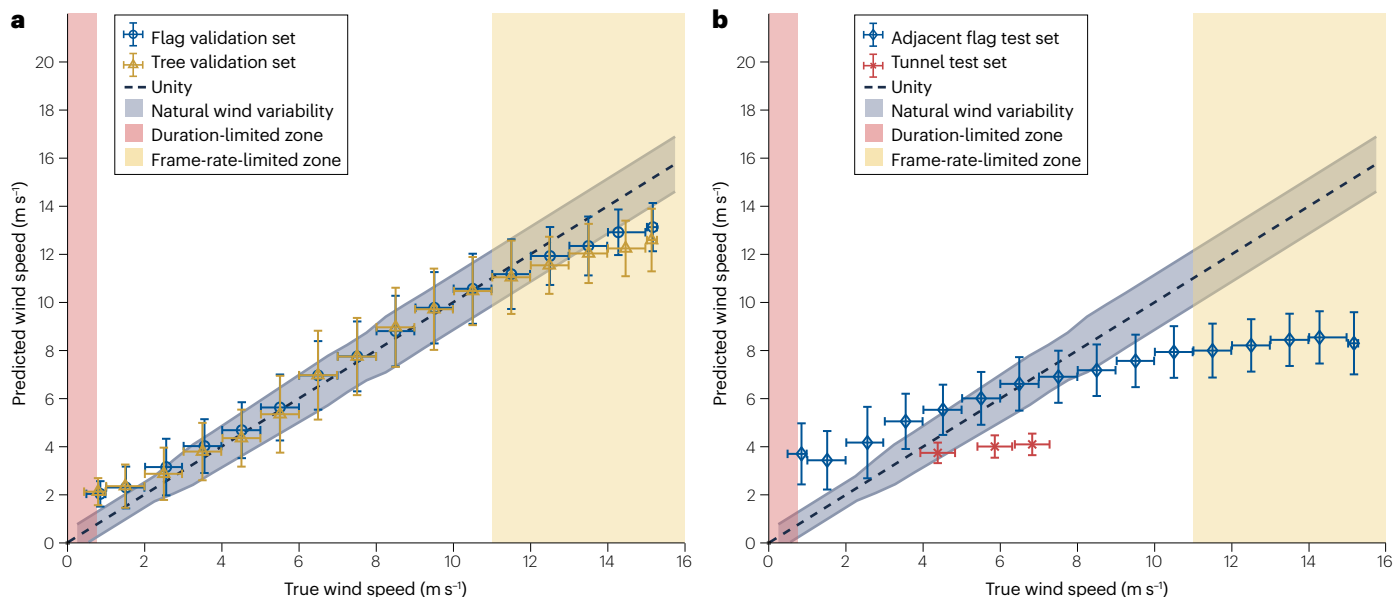


Fig. 2 | Data-driven implementation of visual anemometry based on measurements collected at a research field site and in a laboratory wind tunnel. a, A combined convolutional neural network and long short-term memory network successfully predicted the wind speed corresponding to

new videos of the same structures included in the training data set. **b,** Significantly lower sensitivity to wind speed was observed for videos of structures not included in the training data set. Figure adapted with permission from ref. 77, Curran Associates, Inc.

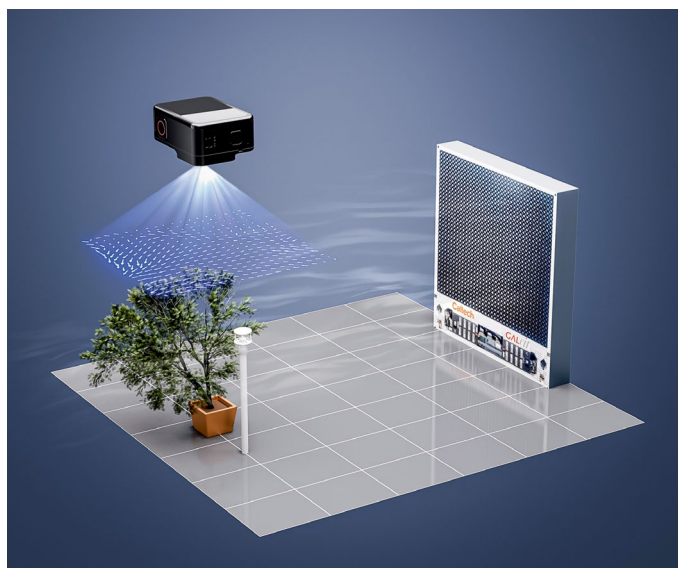


Fig. 3 | Large-scale wind tunnel measurements of vegetation under controlled wind conditions. A 3-m × 3-m array of 1,296 individually addressable fans (right) generates wind conditions with user-defined spatiotemporal profiles and mean speeds up to 20 m s⁻¹. Vegetation exposed to the wind is recorded from above using a high-speed camera. Spatial cross-correlation of successive images reveals the local, instantaneous displacement of the vegetation, illustrated in the planar vector field above the vegetation. Next to the vegetation, a sonic anemometer (white) measures the local wind speed for comparison to visual anemometry.

The motion of the vegetation can be similarly quantified using the Weibull distribution. Cross-correlation of successive images of the moving canopy creates a displacement vector map⁸⁵ representing the spatial distribution of motion induced by the incident wind (vector map above tree in Fig. 3). A quantile–quantile⁸⁴ analysis confirmed that the time series of the spatially averaged canopy motion can be reasonably approximated by a Weibull distribution with its own scale and shape factors, C_1^{canopy} and C_2^{canopy} , respectively.

The dependence of the canopy scale and shape factor on the corresponding wind factors may provide a framework to achieve generalizable visual anemometry. For example, Fig. 4 shows that the various vegetations studied to date all exhibit a similar, sigmoidal dependence of the canopy scale factor, $\tilde{C}_1^{\text{canopy}}$, on the wind scale factor, \tilde{C}_v , in which the tilde denotes a vegetation-specific normalization based on the width, height and centre of each sigmoid curve⁸².

The physical interpretation of this apparently ‘universal’ curve shape can be understood by recalling the scale factor as a surrogate for the mean speed of the wind and canopy. At relatively low wind speeds, the dynamic pressure exerted by the wind on the canopy elements may be insufficient to overcome the inertia and elastic restoring force of the structures exposed to wind. In this regime, the slope of the curve in Fig. 4 is expected to be nearly zero. At sufficiently high-wind speeds, the resistance of the canopy to motion is overcome, and further increases in wind speed correspond to a proportional increase in canopy motion (that is, the region of linear slope in Fig. 4). At high-wind speeds, further deflection of the canopy structures is limited by the fixed position of the vegetation roots in the substrate below. This constraint is reflected in the plateau of $\tilde{C}_1^{\text{canopy}}$ at large values of normalized wind scale factor \tilde{C}_v in Fig. 4.

A key implication of the sigmoidal response curve is that its slope – a measure of the sensitivity of canopy motion to changes in the incident wind speed – has regimes at both low and high winds wherein visual anemometry may be fundamentally challenged by the lack of a distinct structural response to wind dynamics. Where the response curve has zero slope, it is not possible to accomplish visual anemometry on the basis of the curve of canopy scale versus wind scale.

The location and width of each of these regions as a function of the dimensional wind speed (in m s⁻¹, for example) are a characteristic of each vegetation type. Placement of a given vegetation type onto the universal curve in Fig. 4 requires a priori knowledge of the incident wind corresponding to each canopy measurement. Generalized visual anemometry would therefore require a means to predict the placement of a given structure onto the universal curve. Additional information based on the shape factor of the motion distribution ($\tilde{C}_2^{\text{canopy}}$), the visual appearance of the structure, comparison with nearby, similar structures in a canopy (as discussed in the section on Energy-based methods), fine-scale changes such as leaf reconfiguration (as discussed in the section on flexibility and reconfiguration) or other statistical priors could be useful for achieving this goal. Two physically motivated priors related to the wind itself include the expected wind speed distribution as a Weibull probability distribution function, and diurnal and seasonal variations in wind that can be known a priori for a given geographic location. Deep learning models that incorporate such physics-based constraints have been widely used in other areas of physics in recent years⁸⁶.

In the regime of high winds, previous work has also observed that canopy motions can be limited by reaching the maximum physical displacement of the structure⁴⁷. Importantly, the absolute turbulence level (in terms of dimensional wind speed fluctuations) is also the highest in the high-wind regime. Hence, measurements of the time-averaged canopy motion (Fig. 4) could be complemented by consideration of the temporal fluctuations in canopy motion to disambiguate the kinetic energy trends in high-wind-speed conditions.

The spatial scale of measurements in a wind tunnel campaign is limited by the size of the individual trees that could be tested in that facility. A wider range of spatiotemporal scales present in the flow through larger canopies can facilitate the incorporation of additional dynamics, such as the ‘honami’ discussed in the section on Energy-based methods, to further constrain estimates of the wind incident on a canopy.

Outlook

We conclude with a prospective discussion of three research avenues that could accomplish the necessary model closure for generalized visual anemometry.

New data sources

A data-driven approach to generalized visual anemometry could use the discovered universal curve as a statistical prior in a physics-informed machine learning framework. This approach anticipates that measurements collected without ground-truth wind speed measurements should exhibit a scale factor relationship between the wind and canopy distributions that is sigmoidal (Fig. 4). The relationships between the wind and canopy shape factors may provide additional physical constraints to enable a data-driven model that can extrapolate beyond its training data set.

To be sure, this approach does not obviate the need for comprehensive data collection to train the neural networks or other

machine-learning representations of the underlying physics. However, there exists a growing set of data sources that could be leveraged for this purpose. These include open-source, near-ground imagery⁸⁷, coming from sources such as long-term ecological measurement campaigns^{88–93}, hazard monitoring systems such as those deployed for wildfire detection^{94–102} and, in the built environment, traffic and security cameras^{103,104}. A large number of existing meteorological measurement campaigns could also be augmented with concurrent video collection to provide large volumes of new labelled data to train machine learning models^{105–115}.

Emerging commercial satellite data feeds can provide a potentially transformative data source if extended to time-resolved imagery, as the wide area coverage and frequent revisits of remote locations provide data that are inaccessible by other means^{99,116}. Although the distant vantage of satellite data can limit the spatial and temporal resolution of near-ground canopy measurements, recent advances in artificial intelligence-based image upscaling could enable features of the canopy essential for visual anemometry to be recovered from low-resolution data following initial training from benchmark data sets¹¹⁷.

New computational tools

The two primary approaches towards visual anemometry that have been explored in this Perspective article – first-principles physical modelling and data-driven machine learning – have both been considered thus far from a point of view that depends on empirical measurements of the relevant flow–structure interactions. Advances in high-performance computing now make it feasible to achieve physically realistic computational simulations of wind interactions with geometrically complex structures such as vegetation^{118–121}. Hence, another promising route to generalized visual anemometry could use simulations to complement the aforementioned field measurement campaigns.

Numerical simulations provide the added benefit of enabling complex details of environmental structures, such as the branches of a tree, to be tracked with high spatiotemporal fidelity. Because imagery from cameras provides only a 2D projection of the 3D structure kinematics, the set of parameters used to describe the canopy is limited to quantities derived from that projection. The canopy motion determined from image cross-correlation is one example (Fig. 3). By contrast, numerical simulations could provide 3D kinematic data, from which a richer set of physical descriptors could be derived to quantify the canopy response to incident wind. That higher-dimensional description can better delineate different modes of structural response and could also be used for the task of identifying and classifying structures of interest in a machine learning context. Accurate simulations of wind response can also be used in virtual reality and gaming contexts, which can potentially engage a broader audience in efforts to crowdsource measurements for visual anemometry training data¹²⁰.

New physics

The ultimate solution to the challenge of generalized visual anemometry may lie in a combined strategy that leverages knowledge of canonical flow–structure interactions, such as those introduced in this Perspective article, along with libraries of representative wind interactions from empirical observations and from analogous computational models. However, the most exciting role for the physics community may lie in a third approach: the discovery and development of new physics concepts that augment existing knowledge of the nature of flow–structure interactions as well as remote-sensing capabilities.

Although the flow–structure interactions to be exploited by visual anemometry are a manifestation of classical mechanics – a subfield of physics that is ostensibly mature in comparison to, say, quantum science – knowledge of those physics is still limited to a relatively small set of simplified geometries. The appeal in this Perspective article to objects with circular cross-sections, slender or planar geometries and moderate elasticity was by necessity, as established models for the physics of flow–structure interactions have not evolved beyond those relatively simple configurations despite intensive study for more than a century^{122–131}. A historical limitation on the study of flow-induced motion of more complex structures was the inability to visualize the associated fluid–solid interactions with high spatiotemporal resolution. However, the advent of high-speed laser velocimetry^{132,133}, 3D flow tomography^{128,134} and algorithms to compute the pressure field corresponding to flow velocity measurements^{135,136} now makes it possible for experimental physicists to revisit the classical mechanics in geometric configurations, approaching the complexity of structures relevant for visual anemometry. Indeed, important new results have emerged in recent years, from plant-scale to canopy-scale, which have improved our understanding of flow–structure interactions and which bring the present goal of generalized visual anemometry closer to realization^{70,137}.

Modern model reduction techniques from dynamical systems theory^{138–140} have the potential to distill high-dimensional data sets such as those derived from new experimental measurements. Physicists familiar with the challenge of dimensionality reduction in other areas of nonlinear dynamics could apply many of the same tools here. Simplified kinematic motifs of the observed structure motion, extracted using model reduction, may prove to be robust correlates of the incident wind speed and direction. Those motifs could also provide a target for unsupervised machine learning approaches that aim to classify or even deduce material properties of objects in the wind based solely on their observed motion.

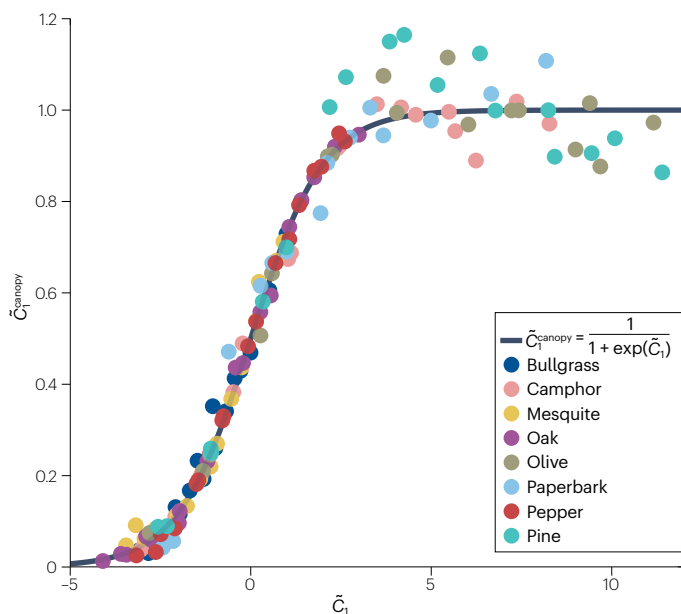


Fig. 4 | Compilation of visual anemometry measurements of eight vegetation species. Data are plotted in terms of the normalized canopy scale factor, $\tilde{C}_1^{\text{canopy}}$, against normalized wind scale factor, \tilde{C}_1 . Black curve corresponds to the sigmoid equation. Data derived from ref. 82.

Although the concept of visual anemometry took initial inspiration from our human powers of visual observation, the spectrum of visible light represents a relatively small band of the electromagnetic radiation that is absorbed, reflected and emitted by both natural and engineered objects that could be used for visual anemometry. The range of applications of the concepts introduced here could be further expanded by physicists interested in exploring the broader spectrum of electromagnetic radiation associated with objects covering the surface of the Earth that are subjected to local winds. An immediate example is infrared radiation, which could enable visual anemometry measurements at night. Imaging at longer wavelengths, such as millimetre-wave imaging^{141–143}, could also potentially be used to circumvent optical interference such as cloud cover, provided that the spatial resolution of those measurements still enables structural motions to be resolved. Additional optical properties, such as the polarization of reflected light, could be used to infer not only translational motion of objects but also changes in object orientation associated with flow-induced bending and torsion of reflective surfaces¹⁴⁴ such as leaves and blades of grass. These signatures could provide additional means to discriminate between regimes of flow speed and direction incident on the objects.

Finally, it is important to recall that 70% of the surface of the Earth is covered by water. Inference of wind fields near the ocean surface is confounded by the more complex deformations associated with the air–water interface^{144–147}. This complexity presents not only challenges but also opportunities. For example, the high-wind plateau in structural response observed for ground-mounted structures (Fig. 4) need not limit correlations between ocean surface deformation and wind speed in similarly high-wind regimes. Hence, a larger range of wind speeds may be accessible to visual anemometry over the ocean when compared with the method applied on land. In addition, ocean measurements can potentially use not only the kinematics of the air–water interface but also the wind-induced motion of ocean spray above the surface¹⁴⁸ and the water-induced motion of submerged vegetation^{126,127,149}.

This list is merely illustrative of avenues for new contributions from the physics community. Our goal is that our discussion of the opportunities and challenges associated with visual anemometry will encourage the reader to pursue one or more of these research directions. Visual anemometry provides a unique opportunity for the physics community to contribute to various important and far-reaching topics in global sustainability.

Published online: 22 August 2023

References

- Wanninkhof, R. & McGillis, W. R. A cubic relationship between air–sea CO₂ exchange and wind speed. *Geophys. Res. Lett.* **26**, 1889–1892 (1999).
- King, A. W. et al. North America's net terrestrial CO₂ exchange with the atmosphere 1990–2009. *Biogeosciences* **12**, 399–414 (2015).
- Casas-Ruiz, J. P. et al. Integrating terrestrial and aquatic ecosystems to constrain estimates of land–atmosphere carbon exchange. *Nat. Commun.* **14**, 1571 (2023).
- Wanninkhof, R. Relationship between wind speed and gas exchange over the ocean. *J. Geophys. Res.* **97**, 7373 (1992).
- Pereira, R., Ashton, I., Sabbaghzadeh, B., Shutler, J. D. & Upstill-Goddard, R. C. Reduced air–sea CO₂ exchange in the Atlantic Ocean due to biological surfactants. *Nat. Geosci.* **11**, 492–496 (2018).
- Upstill-Goddard, R. C. Air–sea gas exchange in the coastal zone. *Estuar. Coast. Shelf Sci.* **70**, 388–404 (2006).
- Pithan, F. et al. Role of air–mass transformations in exchange between the Arctic and mid-latitudes. *Nat. Geosci.* **11**, 805–812 (2018).
- Siegenthaler, U. & Sarmiento, J. L. Atmospheric carbon dioxide and the ocean. *Nature* **365**, 119–125 (1993).
- Huffman, J. A. et al. High concentrations of biological aerosol particles and ice nuclei during and after rain. *Atmos. Chem. Phys.* **13**, 6151–6164 (2013).
- Burrows, F. M. Wind-borne seed and fruit movement. *N. Phytol.* **75**, 405–418 (1975).
- Horn, H. S., Nathan, R. A. N. & Kaplan, S. R. Long-distance dispersal of tree seeds by wind. *Ecol. Res.* **16**, 877–885 (2001).
- Okubo, A. & Levin, S. A. A theoretical framework for data analysis of wind dispersal of seeds and pollen. *Ecology* **70**, 329–338 (1989).
- de Langre, E. Effects of wind on plants. *Annu. Rev. Fluid Mech.* **40**, 141–168 (2008).
- Nathan, R. et al. Mechanisms of long-distance dispersal of seeds by wind. *Nature* **418**, 409–413 (2002).
- Butler, R. W., Williams, T. D., Warnock, N. & Bishop, M. A. Wind assistance: a requirement for migration of shorebirds? *Auk* **114**, 456–466 (1997).
- Canham, R., Flemming, S. A., Hope, D. D. & Drever, M. C. Sandpipers go with the flow: correlations between estuarine conditions and shorebird abundance at an important stopover on the Pacific Flyway. *Ecol. Evol.* **11**, 2828–2841 (2021).
- Drake, V. A. & Farrow, R. A. The influence of atmospheric structure and motions on insect migration. *Annu. Rev. Entomol.* **33**, 183–210 (1988).
- Burton, T., Jenkins, N., Sharpe, D. & Bossanyi, E. Wind energy handbook. *Wind. Eng.* **25**, 197–199 (2011).
- Veers, P. et al. Grand challenges in the science of wind energy. *Science* **366**, eaau2027 (2019).
- Clifton, A., Barber, S., Stökl, A., Frank, H. & Karlsson, T. Research challenges and needs for the deployment of wind energy in hilly and mountainous regions. *Wind. Energy Sci.* **7**, 2231–2254 (2022).
- Stanislawski, B. J., Harman, T., Silverman, T. J., Cal, R. B. & Calaf, M. Row spacing as a controller of solar module temperature and power output in solar farms. *J. Renew. Sustain. Energy* **14**, 063702 (2022).
- Smith, S. E. et al. Viewing convection as a solar farm phenomenon broadens modern power predictions for solar photovoltaics. *J. Renew. Sustain. Energy* **14**, 063502 (2022).
- Hart, C. Mediaeval kites and windsocks. *Aeronaut. J.* **73**, 1019–1026 (1969).
- Kaimal, J. C. & Finnigan, J. J. Atmospheric boundary layer flows: their structure and measurement. *Book* **72**, 289 (1994).
- Zhang, Y., Yuan, J., Wu, Y., Dong, J. & Xia, H. Sub-meter wind detection with pulsed coherent Doppler lidar. *Phys. Rev. Fluids* **8**, L022701 (2023).
- Baker, R. C. Flow measurement handbook: industrial designs, operating principles, performance, and applications. *Flow Measurement Handbook* <https://doi.org/10.1017/CBO9780511471100> (Cambridge Univ. Press, 2000).
- Goymer, P. A trillion trees. *Nat. Ecol. Evol.* **2**, 208–209 (2018).
- Parkinson, G. V. Wind-induced instability of structures. *Philos. Trans. R. Soc. A.* **269**, 395–413 (1971).
- Simpson, G. C. *The Velocity Equivalents of the Beaufort Scale* (HM Stationery Office, 1926).
- Jemison, G. Beaufort scale of wind force as adapted for use on forested area of the northern Rocky Mountains. *J. Sci.* **49**, 77–82 (1934).
- Doswell, C. A., Brooks, H. E. & Dotzek, N. On the implementation of the enhanced Fujita scale in the USA. *Atmos. Res.* **93**, 554–563 (2009).
- Wade, J. E. & Hewson, E. W. Trees as a local climatic wind indicator. *J. Appl. Meteorol.* **18**, 1182–1187 (1979).
- Tropea, C., Yarin, A. L. & Foss, J. F. *Springer Handbook of Experimental Fluid Mechanics* (Springer Science+Business Media, 2007).
- Britter, R. E. & Hanna, S. R. Flow and dispersion in urban areas. *Annu. Rev. Fluid Mech.* **35**, 469–496 (2003).
- Finnigan, J. Turbulence in plant canopies. *Annu. Rev. Fluid Mech.* **32**, 519–571 (2000).
- Belcher, S. E., Harman, I. N. & Finnigan, J. J. The wind in the willows: flows in forest canopies in complex terrain. *Annu. Rev. Fluid Mech.* **44**, 479–504 (2012).
- Nepf, H. M. Flow and transport in regions with aquatic vegetation. *Annu. Rev. Fluid Mech.* **44**, 123–142 (2012).
- Gunn, D. J. & Malik, A. A. Wind forces and the proximity of cooling towers to each other. *Nature* **210**, 1142–1143 (1966).
- McCroskey, W. J. Unsteady airfoils. *Annu. Rev. Fluid Mech.* **14**, 285–311 (1982).
- Hartog, J. P. D. Transmission line vibration due to sleet. *Trans. Am. Inst. Electr. Eng.* **51**, 1074–1076 (1932).
- Nikitas, N. & Macdonald, J. H. G. Misconceptions and generalizations of the Den Hartog galloping criterion. *J. Eng. Mech.* **140**, 04013005 (2014).
- Gosselin, F. P. Mechanics of a plant in fluid flow. *J. Exp. Bot.* **70**, 3533–3548 (2019).
- Alben, S., Shelley, M. & Zhang, J. Drag reduction through self-similar bending of a flexible body. *Nature* **420**, 479–481 (2002).
- Gosselin, F., de Langre, E. & Machado-Almeida, B. A. Drag reduction of flexible plates by reconfiguration. *J. Fluid Mech.* **650**, 319–341 (2010).
- Vogel, S. Drag and reconfiguration of broad leaves in high winds. *J. Exp. Bot.* **40**, 941–948 (1989).
- Vogel, S. *Life in Moving Fluids: The Physical Biology of Flow* (Princeton Univ. Press, 1994).
- Tadrist, L. et al. Foliage motion under wind, from leaf flutter to branch buffeting. *J. R. Soc. Interface* **15**, 20180010 (2018).
- Koehl, M. A. R. Effects of sea anemones on the flow forces they encounter. *J. Exp. Biol.* **69**, 87–105 (1977).
- Vogel, S. Drag and flexibility in sessile organisms. *Am. Zool.* **24**, 37–44 (1984).
- Gardiner, B., Berry, P. & Moulia, B. Review: wind impacts on plant growth, mechanics and damage. *Plant. Sci.* **245**, 94–118 (2016).
- Niklas, K. Differences between *Acer saccharum* leaves from open and wind-protected sites. *Ann. Bot.* **78**, 61–66 (1996).

52. Jaffe, M. J. Thigmomorphogenesis: the response of plant growth and development to mechanical stimulation. *Planta* **114**, 143–157 (1973).
53. Gipe, P. Wind Power. *Wind. Eng.* **28**, 629–631 (2004).
54. Cardona, J. L., Bouman, K. L. & Dabiri, J. O. Wind speed inference from environmental flow–structure interactions. *Flow* **1**, E4 (2021).
55. Bouman, K. L., Xiao, B., Battaglia, P. & Freeman, W. T. Estimating the material properties of fabric from video. 2013 *IEEE International Conference on Computer Vision* 1984–1991 (IEEE, 2013); <https://doi.org/10.1109/ICCV.2013.455>.
56. Runia, T. F. H., Gavriluyk, K., Snoek, C. G. M. & Smeulders, A. W. M. Cloth in the wind: a case study of physical measurement through simulation. *Proceedings of the IEEE/CVF Conference on Computer Vision and Pattern Recognition* 10498–10507 (IEEE, 2020).
57. de Langre, E. Plant vibrations at all scales: a review. *J. Exp. Bot.* **70**, 3521–3531 (2019).
58. Cardona, J. L. & Dabiri, J. O. Wind speed inference from environmental flow–structure interactions, part 2: leveraging unsteady kinematics. Preprint at <https://doi.org/10.48550/arXiv.2107.09784> (2021).
59. Shao, C.-P., Chen, Y.-J. & Lin, J.-Z. Wind induced deformation and vibration of a *Platanus acerifolia* leaf. *Acta Mech. Sin.* **28**, 583–594 (2012).
60. Sun, J. J. et al. Self-supervised keypoint discovery in behavioral videos. 2022 *IEEE/CVF Conference on Computer Vision and Pattern Recognition (CVPR)* 2161–2170 (IEEE, 2022).
61. Betz, A. Das maximum der theoretisch möglichen auswendung des windes durch windmotoren. *Z. gesamte Turbinewesen* **26**, 307–309 (1920).
62. Dabiri, J. O. Theoretical framework to surpass the Betz limit using unsteady fluid mechanics. *Phys. Rev. Fluids* **5**, 022501 (2020).
63. Lu, S. S. & Willmarth, W. W. Measurements of the structure of the Reynolds stress in a turbulent boundary layer. *J. Fluid Mech.* **60**, 481–511 (1973).
64. Stull, R. B. *An Introduction to Boundary Layer Meteorology* Book 13 (Springer Netherlands, 1988).
65. Bossuyt, J., Howland, M. F., Meneveau, C. & Meyers, J. Measurement of unsteady loading and power output variability in a micro wind farm model in a wind tunnel. *Exp. Fluids* **58**, 1 (2017).
66. Py, C., de Langre, E., Mouliat, B. & Hémon, P. Measurement of wind-induced motion of crop canopies from digital video images. *Agric. For. Meteorol.* **130**, 223–236 (2005).
67. Py, C., De Langre, E. & Mouliat, B. A frequency lock-in mechanism in the interaction between wind and crop canopies. *J. Fluid Mech.* **568**, 425 (2006).
68. Rodriguez, M., Ploquin, S., Mouliat, B. & de Langre, E. The multimodal dynamics of a walnut tree: experiments and models. *J. Appl. Mech.* **79**, 044505 (2012).
69. Barbacci, A. et al. A robust videogrametric method for the velocimetry of wind-induced motion in trees. *Agric. For. Meteorol.* **184**, 220–229 (2014).
70. Tadriss, L., Julio, K., Saudreau, M. & de Langre, E. Leaf flutter by torsional galloping: experiments and model. *J. Fluids Struct.* **56**, 1–10 (2015).
71. DGS. *California Building Standards Commission*. <https://www.dgs.ca.gov/BSC/Codes> (2022).
72. Ching, F. D. K. & Winkel, S. R. *Building Codes Illustrated: A Guide to Understanding the 2018 International Building Code* (International Code Council, 2018).
73. Gönen, T. *Electrical Power Transmission System Engineering: Analysis and Design* 1066 (John Wiley & Sons, 2009).
74. Metwally, I. High-voltage power cables plug into the future. *IEEE Potentials* **27**, 18–25 (2008).
75. *Springer Handbook of Power Systems* (Springer Singapore, 2021).
76. Gockenbach, E. High voltage engineering. In *Springer Handbooks* 131–182 (Springer Science and Business Media Deutschland GmbH, 2021).
77. Cardona, J. L., Howland, M. F. & Dabiri, J. O. Seeing the wind: visual wind speed prediction with a coupled convolutional and recurrent neural network. In *33rd Conference on Neural Information Processing Systems (NeurIPS 2019)* (eds Wallach, H. et al.) (Curran Associates, Inc., 2019).
78. Zhang, Q., Xu, J., Crane, M. & Luo, C. See the wind: wind scale estimation with optical flow and VisualWind dataset. *Sci. Total. Environ.* **846**, 157204 (2022).
79. Zhang, Q., Xu, J., Crane, M. & Luo, C. Visualwind: a novel video dataset for cameras to sense the wind. In *IGARSS 2022 – 2022 IEEE International Geoscience and Remote Sensing Symposium* (IEEE, 2022).
80. Deng, J. et al. ImageNet: a large-scale hierarchical image database. In *2009 IEEE Conference on Computer Vision and Pattern Recognition* 248–255 (IEEE, 2009).
81. Lin, T.-Y. et al. Microsoft COCO: common objects in context. In *Lecture Notes in Computer Science (Including Subseries Lecture Notes in Artificial Intelligence and Lecture Notes in Bioinformatics)* 8693 LNCS, 740–755 (Springer Verlag, 2014).
82. Goldshmid, R. H. & Dabiri, J. O. Visual anemometry measurements of eight vegetation species. *CaltechDATA* <https://doi.org/10.22002/crb7k-1gj48> (2023).
83. Tuller, S. E. & Brett, A. C. The characteristics of wind velocity that favor the fitting of a Weibull distribution in wind speed analysis. *J. Clim. Appl. Meteorol.* **23**, 124–134 (1984).
84. Wilk, M. B. & Gnanadesikan, R. Probability plotting methods for the analysis of data. *Biometrika* **55**, 1 (1968).
85. Thielicke, W. & Sonntag, R. Particle image velocimetry for MATLAB: accuracy and enhanced algorithms in PIVlab. *J. Open. Res. Softw.* **9**, 12 (2021).
86. Karniadakis, G. E. et al. Physics-informed machine learning. *Nat. Rev. Phys.* **3**, 422–440 (2021).
87. Beyer, R. A., Alexandrov, O. & McMichael, S. The Ames Stereo Pipeline: NASA's open source software for deriving and processing terrain data. *Earth Space Sci.* **5**, 537–548 (2018).
88. Beery, S. et al. The Auto Arborist Dataset: a large-scale benchmark for multiview urban forest monitoring under domain shift. In *2022 IEEE/CVF Conference on Computer Vision and Pattern Recognition (CVPR)* 21262–21275 (IEEE, 2022).
89. Harris, G., Thompson, R., Childs, J. L. & Sanderson, J. G. Automatic storage and analysis of camera trap data. *Bull. Ecol. Soc. Am.* **91**, 352–360 (2010).
90. Newey, S. et al. Limitations of recreational camera traps for wildlife management and conservation research: a practitioner's perspective. *Ambio* **44**, 624–635 (2015).
91. Hamel, S. et al. Towards good practice guidance in using camera-traps in ecology: influence of sampling design on validity of ecological inferences. *Methods Ecol. Evol.* **4**, 105–113 (2013).
92. Hentati-Sundberg, J. et al. Seabird surveillance: combining CCTV and artificial intelligence for monitoring and research. *Remote Sens. Ecol. Conserv.* <https://doi.org/10.1002/rse2.329> (2023).
93. Chen, R., Little, R., Mihaylova, L., Delahay, R. & Cox, R. Wildlife surveillance using deep learning methods. *Ecol. Evol.* **9**, 9453–9466 (2019).
94. Gupta, V., Roy, S., Jaiswal, V., Bhardwaj, K. & Rana, P. S. Drone assisted deep learning based wildfire detection system. In *2022 Seventh International Conference on Parallel, Distributed and Grid Computing (PDGC)* 162–166 (IEEE, 2022).
95. Çetin, A. E. et al. Video fire detection – review. *Digit. Signal Process.* **23**, 1827–1843 (2013).
96. Agirman, A. K. & Tasdemir, K. BLSTM based night-time wildfire detection from video. *PLoS ONE* **17**, e0269161 (2022).
97. Shamsoshoara, A. et al. Aerial imagery pile burn detection using deep learning: the FLAME dataset. *Computer Netw.* **193**, 108001 (2021).
98. Saponara, S., Elhanashi, A. & Gagliardi, A. Real-time video fire/smoke detection based on CNN in antifire surveillance systems. *J. Real. Time Image Process.* **18**, 889–900 (2021).
99. de Almeida Pereira, G. H., Fusioka, A. M., Nassu, B. T. & Minetto, R. Active fire detection in Landsat-8 imagery: a large-scale dataset and a deep-learning study. *ISPRS J. Photogramm. Remote. Sens.* **178**, 171–186 (2021).
100. Zhang, G., Wang, M. & Liu, K. Forest fire susceptibility modeling using a convolutional neural network for Yunnan Province of China. *Int. J. Disaster Risk Sci.* **10**, 386–403 (2019).
101. Zhang, Q., Xu, J., Xu, L. & Guo, H. Deep convolutional neural networks for forest fire detection. In *Proceedings of the 2016 International Forum on Management, Education and Information Technology Application* <https://doi.org/10.2991/ifmeita-16.2016.105> (Atlantis Press, 2016).
102. Mahdi, A. S. & Mahmood, S. A. Analysis of deep learning methods for early wildfire detection systems: review. In *2022 5th International Conference on Engineering Technology and its Applications (IICETA)* 271–276 (IEEE, 2022).
103. Eamthanakul, B., Ketcham, M. & Chumua, N. The traffic congestion investigating system by image processing from CCTV camera. In *2017 International Conference on Digital Arts, Media and Technology (CDAMT)* 240–245 (IEEE, 2017).
104. Shah, A. P., Lamare, J.-B., Nguyen-Anh, T. & Hauptmann, A. CADP: a novel dataset for CCTV traffic camera based accident analysis. In *2018 15th IEEE International Conference on Advanced Video and Signal Based Surveillance (AVSS)* 1–9 (IEEE, 2018).
105. Fernando, H. J. S. et al. The MATERHORN: unraveling the intricacies of mountain weather. *Bull. Am. Meteorol. Soc.* **96**, 1945–1967 (2015).
106. Goldshmid, R. H. & Liberzon, D. Obtaining turbulence statistics of thermally driven anabatic flow by sonic-hot-film combo anemometer. *Environ. Fluid Mech.* **20**, 1221–1249 (2018).
107. Stull, R. B. & Eloranta, E. W. Boundary layer experiment – 1983. *Bull. Am. Meteorol. Soc.* **65**, 450–456 (1984).
108. Holtslag, B. GEWEX atmospheric boundary-layer study (GABLS) on stable boundary layers. *Bound. Layer Meteorol.* **118**, 243–246 (2006).
109. Rajewski, D. A. et al. Crop wind energy experiment (CWEX): observations of surface-layer, boundary layer, and mesoscale interactions with a wind farm. *Bull. Am. Meteorol. Soc.* **94**, 655–672 (2013).
110. Wilczak, J. et al. The wind forecast improvement project (WFIP): a public–private partnership addressing wind energy forecast needs. *Bull. Am. Meteorol. Soc.* **96**, 1699–1718 (2015).
111. Shaw, W. J. et al. The Second Wind Forecast Improvement Project (WFIP2): general overview. *Bull. Am. Meteorol. Soc.* **100**, 1687–1699 (2019).
112. Allwine, K. J. & Flaherty, J. E. *Joint Urban 2003: Study Overview and Instrument Locations*. <http://www.osti.gov/servlets/purl/890732-i6tMLI/> <https://doi.org/10.2172/890732> (2006).
113. Moriarty, P. et al. American WAKE Experiment (AWAKEN). <https://www.osti.gov/servlets/purl/1659798/> <https://doi.org/10.2172/1659798> (2020).
114. Fernando, H. J. S. et al. The Perdigoão: peering into microscale details of mountain winds. *Bull. Am. Meteorol. Soc.* **100**, 799–819 (2019).
115. Poulos, G. S. et al. CASES-99: a comprehensive investigation of the stable nocturnal boundary layer. *Bull. Am. Meteorol. Soc.* **83**, 555–581 (2002).
116. Alkhatib, A. A. A review on forest fire detection techniques. *Int. J. Distrib. Sens. Netw.* **10**, 597368 (2014).
117. Ignatov, A. et al. Real-time video super-resolution on smartphones with deep learning, mobile AI 2021 challenge: report. In *Proceedings of the IEEE/CVF Conference on Computer Vision and Pattern Recognition* 2535–2544 (IEEE, 2021).
118. Disney, M., Lewis, P. & Saich, P. 3D modelling of forest canopy structure for remote sensing simulations in the optical and microwave domains. *Remote Sens. Environ.* **100**, 114–132 (2006).
119. Quigley, E., Yu, Y., Huang, J., Lin, W. & Fedkiw, R. Real-time interactive tree animation. *IEEE Trans. Vis. Comput. Graph.* **24**, 1717–1727 (2018).

120. Pirk, S., Niese, T., Hädrich, T., Benes, B. & Deussen, O. Windy trees: computing stress response for developmental tree models. *ACM Trans. Graph.* **33**, 204 (2014).
121. He, S., Liu, H. & Shen, L. Simulation-based study of turbulent aquatic canopy flows with flexible stems. *J. Fluid Mech.* **947**, A33 (2022).
122. Dowell, E. H. & Hall, K. C. Modeling of fluid–structure interaction. *Annu. Rev. Fluid Mech.* **33**, 445–490 (2001).
123. Parameshwaran, R., Dhulipalla, S. J. & Yendluri, D. R. Fluid–structure interactions and flow induced vibrations: a review. *Procedia Eng.* **144**, 1286–1293 (2016).
124. Mossa, M. et al. Quasi-geostrophic jet-like flow with obstructions. *J. Fluid Mech.* **921**, A12 (2021).
125. De Serio, F. et al. Turbulent jet through porous obstructions under Coriolis effect: an experimental investigation. *Exp. Fluids* **62**, 218 (2021).
126. Lowe, R. J., Koseff, J. R. & Monismith, S. G. Oscillatory flow through submerged canopies: 1. Velocity structure. *J. Geophys. Res. Ocean.* **110**, 1–17 (2005).
127. Lowe, R. J., Shavit, U., Falter, J. L., Koseff, J. R. & Monismith, S. G. Modeling flow in coral communities with and without waves: a synthesis of porous media and canopy flow approaches. *Limnol. Oceanogr.* **53**, 2668–2680 (2008).
128. van Hout, R., Hershkovitz, A., Elsinga, G. E. & Westerweel, J. Combined three-dimensional flow field measurements and motion tracking of freely moving spheres in a turbulent boundary layer. *J. Fluid Mech.* **944**, A12 (2022).
129. Bearman, P. W. Vortex shedding from oscillating bluff bodies. *Annu. Rev. Fluid Mech.* **16**, 195–222 (1984).
130. Lanchester, F. W. *Aerodynamics: Constituting the First Volume of a Complete Work on Aerial Flight* (Constable, 1907).
131. Fage, A. *The Aeroplane: A Concise Scientific Study* (C. Brissin, 1917).
132. Lynch, K. & Scarano, F. A high-order time-accurate interrogation method for time-resolved PIV. *Meas. Sci. Technol.* **24**, 035305 (2013).
133. Taylor, Z. J., Gurka, R., Kopp, G. A. & Liberzon, A. Long-duration time-resolved PIV to study unsteady aerodynamics. *IEEE Trans. Instrum. Meas.* **59**, 3262–3269 (2010).
134. Elsinga, G. E., Scarano, F., Wieneke, B. & van Oudheusden, B. W. Tomographic particle image velocimetry. *Exp. Fluids* **41**, 933–947 (2006).
135. Liu, X. & Katz, J. Instantaneous pressure and material acceleration measurements using a four-exposure PIV system. *Exp. Fluids* **41**, 227–240 (2006).
136. Dabiri, J. O., Bose, S., Gemmell, B. J., Colin, S. P. & Costello, J. H. An algorithm to estimate unsteady and quasi-steady pressure fields from velocity field measurements. *J. Exp. Biol.* **217**, 331–336 (2014).
137. Jin, Y., Kim, J.-T., Fu, S. & Chamorro, L. P. Flow-induced motions of flexible plates: fluttering, twisting and orbital modes. *J. Fluid Mech.* **864**, 273–285 (2019).
138. Kaheman, K., Kutz, J. N. & Brunton, S. L. SINDy-PI: a robust algorithm for parallel implicit sparse identification of nonlinear dynamics. *Proc. R. Soc. A.* **476**, 20200279 (2020).
139. Baddoo, P. J., Herrmann, B., McKeon, B. J., Nathan Kutz, J. & Brunton, S. L. Physics-informed dynamic mode decomposition. *Proc. R. Soc. A.* **479**, 20220576 (2023).
140. Baddoo, P. J., Herrmann, B., McKeon, B. J. & Brunton, S. L. Kernel learning for robust dynamic mode decomposition: linear and nonlinear disambiguation optimization. *Proc. R. Soc. A.* **478**, 20210830 (2022).
141. Racette, P. et al. An airborne millimeter-wave imaging radiometer for cloud, precipitation, and atmospheric water vapor studies. *J. Atmos. Ocean. Technol.* **13**, 610–619 (1996).
142. Mirbeik, A., Ashinoff, R., Jong, T., Aued, A. & Tavassolian, N. Real-time high-resolution millimeter-wave imaging for in-vivo skin cancer diagnosis. *Sci. Rep.* **12**, 4971 (2022).
143. Yujiri, L., Shoucri, M. & Moffa, P. Passive millimeter wave imaging. *IEEE Microw. Mag.* **4**, 39–50 (2003).
144. Ginio, N., Liberzon, D., Lindenbaum, M. & Fishbain, B. Efficient machine learning method for spatio-temporal water surface waves reconstruction from polarimetric images. *Meas. Sci. Technol.* **34**, 055801 (2023).
145. Liberzon, D. & Shemer, L. Experimental study of the initial stages of wind waves' spatial evolution. *J. Fluid Mech.* **681**, 462–498 (2011).
146. Buckley, M. P. & Veron, F. Structure of the airflow above surface waves. *J. Phys. Oceanogr.* **46**, 1377–1397 (2016).
147. Buckley, M. P. & Veron, F. The turbulent airflow over wind generated surface waves. *Eur. J. Mech. B/Fluids* **73**, 132–143 (2019).
148. Veron, F. Ocean spray. *Annu. Rev. Fluid Mech.* **47**, 507–538 (2015).
149. Monismith, S. G. Hydrodynamics of coral reefs. *Annu. Rev. Fluid Mech.* **39**, 37–55 (2007).
150. Larson, E. et al. *Net-zero America: Potential Pathways, Infrastructure, and Impacts* (Princeton Univ., 2020).
151. Sivaram, V., Dabiri, J. O. & Hart, D. M. The need for continued innovation in solar, wind, and energy storage. *Joule* **2**, 1639–1642 (2018).
152. Chow, F. et al. Crossing multiple gray zones in the transition from mesoscale to microscale simulation over complex terrain. *Atmosphere* **10**, 274 (2019).
153. Hilel Goldshmid, R. et al. Separation of upslope flow over a plateau. *Atmosphere* **9**, 165 (2018).
154. Skamarock, W. C. et al. A description of the advanced research WRF model version 4. National Center for Atmospheric Research: Boulder, CO, USA. <https://opensky.ucar.edu/islandora/object/technotes:576/datastream/PDF/download/citation.pdf> (2019).
155. Bodini, N., Hu, W., Optsis, M., Cervone, G. & Alessandrini, S. Assessing boundary condition and parametric uncertainty in numerical-weather-prediction-modeled, long-term offshore wind speed through machine learning and analog ensemble. *Wind. Energy Sci.* **6**, 1363–1377 (2021).
156. Kit, E., Cherkassky, A., Sant, T. & Fernando, H. J. S. In situ calibration of hot-film probes using a collocated sonic anemometer: implementation of a neural network. *J. Atmos. Ocean. Technol.* **27**, 23–41 (2010).
157. Goldshmid, R. H., Winiarska, E. & Liberzon, D. Next generation combined sonic-hotfilm anemometer: wind alignment and automated calibration procedure using deep learning. *Exp. Fluids* **63**, 30 (2022).
158. Kalnay, E. *Atmospheric Modeling, Data Assimilation and Predictability* (Cambridge Univ., 2003).
159. Bauer, P., Thorpe, A. & Brunet, G. The quiet revolution of numerical weather prediction. *Nature* **525**, 47–55 (2015).
160. Cheng, W. Y. Y., Liu, Y., Bourgeois, A. J., Wu, Y. & Haupt, S. E. Short-term wind forecast of a data assimilation/weather forecasting system with wind turbine anemometer measurement assimilation. *Renew. Energy* **107**, 340–351 (2017).
161. Wei, N. J., Brownstein, I. D., Cardona, J. L., Howland, M. F. & Dabiri, J. O. Near-wake structure of full-scale vertical-axis wind turbines. *J. Fluid Mech.* **914**, A17 (2021).
162. Optsis, M., Bodini, N., Debnath, M. & Doubrawa, P. New methods to improve the vertical extrapolation of near-surface offshore wind speeds. *Wind. Energy Sci.* **6**, 935–948 (2021).
163. Kleissl, J. *Solar Energy Forecasting and Resource Assessment* (Academic Press, 2013).
164. Masters, G. *Renewable and Efficient Electric Power Systems* (John Wiley & Sons, 2013).
165. Dupré, O., Vaillon, R. & Green, M. A. *Thermal Behavior of Photovoltaic Devices*. <https://doi.org/10.1007/978-3-319-49457-9> (Springer International Publishing, 2017).
166. Koehl, M., Heck, M., Wiesmeier, S. & Wirth, J. Modeling of the nominal operating cell temperature based on outdoor weathering. *Sol. Energy Mater. Sol. Cell* **95**, 1638–1646 (2011).
167. Schwingshackl, C. et al. Wind effect on PV module temperature: analysis of different techniques for an accurate estimation. *Energy Procedia* **40**, 77–86 (2013).
168. Vaillon, R., Dupré, O., Cal, R. B. & Calaf, M. Pathways for mitigating thermal losses in solar photovoltaics. *Sci. Rep.* **8**, 13163 (2018).
169. Dauxois, T. et al. Confronting grand challenges in environmental fluid mechanics. *Phys. Rev. Fluids* **6**, 020501 (2021).
170. Kareem, A. & Zhou, Y. Gust loading factor — past, present and future. *J. Wind. Eng. Ind. Aerodyn.* **91**, 1301–1328 (2003).
171. Song, J. et al. Natural ventilation in cities: the implications of fluid mechanics. *Build. Res. Inf.* **46**, 809–828 (2018).
172. Bauranov, A. & Rakas, J. Designing airspace for urban air mobility: a review of concepts and approaches. *Prog. Aerosp. Sci.* **125**, 100726 (2021).
173. Cole, K. *Reactive Trajectory Generation and Formation Control for Groups of UAVs in Windy Environments* (George Washington Univ., 2018).
174. García-Sánchez, C., van Beeck, J. & Górlé, C. Predictive large eddy simulations for urban flows: challenges and opportunities. *Build. Env.* **139**, 146–156 (2018).
175. Howland, M. F., Dunbar, O. R. A. & Schneider, T. Parameter uncertainty quantification in an idealized GCM with a seasonal cycle. *J. Adv. Model. Earth Syst.* **14**, e2021MS002735 (2022).
176. Sousa, J., García-Sánchez, C. & Górlé, C. Improving urban flow predictions through data assimilation. *Build. Env.* **132**, 282–290 (2018).
177. Wang, D. et al. Economic footprint of California wildfires in 2018. *Nat. Sustain.* **4**, 252–260 (2020).
178. NOAA National Centers for Environmental Information (NCEI). U.S. billion-dollar weather and climate disasters. *National Centers for Environmental Information* <https://accession.nodc.noaa.gov/0209268> <https://doi.org/10.25921/STKW-7W73> (2023).
179. Turco, M. et al. Exacerbated fires in mediterranean Europe due to anthropogenic warming projected with non-stationary climate-fire models. *Nat. Commun.* **9**, 3821 (2018).
180. Westerling, A. L., Hidalgo, H. G., Cayan, D. R. & Swetnam, T. W. Warming and earlier spring increase western U.S. forest wildfire activity. *Science* **313**, 940–943 (2006).
181. Pimont, F., Dupuy, J.-L., Linn, R. R., Parsons, R. & Martin-St Paul, N. Representativeness of wind measurements in fire experiments: lessons learned from large-eddy simulations in a homogeneous forest. *Agric. For. Meteorol.* **232**, 479–488 (2017).
182. Cheney, N., Gould, J. & Catchpole, W. Prediction of fire spread in grasslands. *Int. J. Wildland Fire* **8**, 1 (1998).
183. Beer, T. The interaction of wind and fire. *Bound. Layer Meteorol.* **54**, 287–308 (1991).
184. Moritz, M. A., Moody, T. J., Krawchuk, M. A., Hughes, M. & Hall, A. Spatial variation in extreme winds predicts large wildfire locations in chaparral ecosystems. *Geophys. Res. Lett.* **37**, 4801 (2010).
185. Rolinski, T. et al. The Santa Ana wildfire threat index: methodology and operational implementation. *Weather Forecast.* **31**, 1881–1897 (2016).
186. Aylor, D. E. The role of intermittent wind in the dispersal of fungal pathogens. *Annu. Rev. Phytopathol.* **28**, 73–92 (1990).
187. Robledo-Arnuncio, J. J. Wind pollination over mesoscale distances: an investigation with Scots pine. *N. Phytol.* **190**, 222–233 (2011).
188. Nathan, R. Long-distance dispersal of plants. *Science* **313**, 786–788 (2006).
189. Brown, J. K. M. & Hovmöller, M. S. Aerial dispersal of pathogens on the global and continental scales and its impact on plant disease. *Science* **297**, 537–541 (2002).
190. Ahmed, S., Compton, S. G., Butlin, R. K. & Gilmartin, P. M. Wind-borne insects mediate directional pollen transfer between desert fig trees 160 kilometers apart. *Proc. Natl Acad. Sci. USA* **106**, 20342–20347 (2009).
191. Muñoz, J., Felicísimo, A. M., Cabezas, F., Burgaz, A. R. & Martínez, I. Wind as a long-distance dispersal vehicle in the southern hemisphere. *Science* **304**, 1144–1147 (2004).
192. Goodwin, M. Pollination of crops in Australia and New Zealand. (2012).

193. Watrud, L. S. et al. Evidence for landscape-level, pollen-mediated gene flow from genetically modified creeping bentgrass with CP4 EPSPS as a marker. *Proc. Natl Acad. Sci. USA* **101**, 14533–14538 (2004).
194. Petit, R. J. & Hampe, A. Some evolutionary consequences of being a tree. *Annu. Rev. Ecol. Evol. Syst.* **37**, 187–214 (2006).
195. Birk, J. H. A broad-spectrum corn herbicide, in a safened formulation, specifically designed for use alone or with glyphosate combinations. *EPA* https://www3.epa.gov/pesticides/chem_search/ppls/007969-00242-20210402.pdf (2015).
196. Nowatzki, J. Understanding air temperature inversions relating to pesticide drift. *NDSU* <https://www.ndsu.edu/agriculture/extension/publications/understanding-air-temperature-inversions-relating-pesticide-drift> (2022).
197. Beckman, B. Pesticide particles can drift afar through inversion phenomenon. *University of Nebraska-Lincoln* <https://cropwatch.unl.edu/2016/pesticide-particles-can-drift-afar-through-inversion-phenomenon> (2016).
198. Beckman, B. Wind speed and herbicide application: integrated crop management. *UNL* <https://crops.extension.iastate.edu/cropnews/2017/01/wind-speed-and-herbicide-application> (2016).
199. Nicolai, D. & Stahl, L. Avoiding herbicide drift. *University of Minnesota* <https://extension.umn.edu/herbicides/too-windy-to-spray#buffer-zones-1040817> (2020).
200. Punia, A. Role of temperature, wind, and precipitation in heavy metal contamination at copper mines: a review. *Environ. Sci. Pollut. Res.* **28**, 4056–4072 (2021).
201. Jiang, Y. & Chen, Q. Study of natural ventilation in buildings by large eddy simulation. *J. Wind. Eng. Ind. Aerodyn.* **89**, 1155–1178 (2001).
202. Chew, L. W., Chen, C. & Górlé, C. Improving thermal model predictions for naturally ventilated buildings using large eddy simulations. *Build. Env.* **220**, 109241 (2022).
203. US Energy Information Administration. Commercial Buildings Energy Consumption Survey, Consumption and Expenditures Highlights. (2018).
204. Linden, P. F. The fluid mechanics of natural ventilation. *Annu. Rev. Fluid Mech.* **31**, 201–238 (1999).
205. Górlé, C. Improving predictions of the urban wind environment using data. *Technology|Architecture+Design* **3**, 137–141 (2019).
206. Aynsley, R. Natural ventilation in passive design. *Environment Design Guide* 1–16 <https://www.jstor.org/stable/26151921> (2014).
207. Gough, H. L. et al. Field measurement of natural ventilation rate in an idealised full-scale building located in a staggered urban array: comparison between tracer gas and pressure-based methods. *Build. Env.* **137**, 246–256 (2018).
208. Chen, C. & Górlé, C. Optimal temperature sensor placement in buildings with buoyancy-driven natural ventilation using computational fluid dynamics and uncertainty quantification. *Build. Env.* **207**, 108496 (2022).
209. Zhong, H.-Y. et al. Single-sided natural ventilation in buildings: a critical literature review. *Build. Env.* **212**, 108797 (2022).

Acknowledgements

The authors gratefully acknowledge seminal contributions from J.L. Cardona in development of several of the concepts presented in this Perspective article, as well as discussions with K. Bouman, J. Sun, Y. Yue and P. Perona at Caltech. Additional helpful discussions occurred in the CV4Ecology Summer Workshop, supported by the Caltech Resnick Sustainability Institute. Constructive feedback from the anonymous reviewers led to meaningful improvements to the presentation of the material in this manuscript. Funding was generously provided by the National Science Foundation (Grant CBET-2019712) and the Center for Autonomous Systems and Technologies at Caltech. Additional support from Heliogen is gratefully acknowledged.

Author contributions

All authors contributed to all aspects of the manuscript.

Competing interests

The authors declare no competing interests.

Additional information

Peer review information *Nature Reviews Physics* thanks Loïc Tadriss and Chunbo Luo for their contribution to the peer review of this work.

Publisher's note Springer Nature remains neutral with regard to jurisdictional claims in published maps and institutional affiliations.

Springer Nature or its licensor (e.g. a society or other partner) holds exclusive rights to this article under a publishing agreement with the author(s) or other rightsholder(s); author self-archiving of the accepted manuscript version of this article is solely governed by the terms of such publishing agreement and applicable law.

© Springer Nature Limited 2023